communications materials

A Nature Portfolio journal

Article

https://doi.org/10.1038/s43246-025-00890-4

Bone mineral platelets are mesocrystals formed by monoclinic nanocrystals

Viktória K. Kis [1,2] ✉, Henry P. Schwarcz[3,4], Nadine Nassif [5] & Zoltán Szekanecz [6]

Detailed multiscale models explain the complex hierarchical structure of bone but the crystal structure and precise organization of bone apatite nanocrystals are unknown. Crystal structure studies of bone mineral are difficult due to intimate structural intergrowth with organic matrix and small crystal size, (2-6 nm x 30-40 nm). Here, we present high resolution transmission electron microscope images of bone mineral platelets, which allow us to clarify both the crystal structure and morphology of bone mineral. We demonstrate that the mineral platelets are polycrystalline mesocrystals with flat faces formed by oriented attachment of several crystals parallel to the **c**-axis and flattened by the dominant (010) prism facets. Individual bone crystals have monoclinic symmetry, in contrast to hydroxyapatite, which is hexagonal. Interestingly, biomimetic apatite also exhibits monoclinic symmetry. These findings provide a plausible explanation for the observed flat platelet morphology of bone crystals, which plays a key role in collagen binding and is at odds with the hexagonal structure and morphology of geological apatites.

Bone is a nanocomposite material made of type I collagen fibrils and a mineral phase, which is believed to be a carbonated apatite. Collagen and bone apatite (BA) crystals are organized into a complex hierarchical architecture from the nano to the macro scale, developing the excellent mechanical properties of bone[1,2]. Synthesis in physiological conditions of materials with similar performance and durability has been proven a challenge up to now[3,4], which partly explains the enhanced and continuous scientific interest towards the sub-micrometer structure and organization of bone.

Understanding the mechanical response of bone requires the consideration of the size, orientation, and local arrangement of the mineral component in the collagen matrix[5,6]. Recent transmission electron microscopic (TEM) studies on cryo ion-beam milled sections of bone allowed us to derive a three-dimensional picture of the organic-inorganic nanocomposite structure (Fig. 1), which opens the way toward a better understanding of bone formation[7]. The mineral component of bone is in the form of platelets 2–6 nm thick and up to 200 nm long. These mineral platelets (MPs) have linear or frequently curved morphology[8], and form stacks, which surround the collagen fibrils (Fig. 1b). Stacks are spaced 30–50 nm apart, consistent with the diameter of the fibril (Fig. 1c)[9–12]. BA crystals show strong [001] (we use three-digit indices (*hkl*) or [*uvw*] for crystallographic notations in case of BA, and we use the traditional four-digit notation (*hkil*), with $-i = h + k$ only in relation to crystal morphology of hexagonal (geological) apatite.) preferred orientation parallel to the collagen fibril. Dispersion of **c**-axes of BA was observed up to ±36° on electron diffraction patterns[9], which could be due to local variation in the orientation of MPs. BA nanocrystals are ~35 nm wide along [001] as determined using the Scherrer equation for annealed human dentin[13] and rat cortical bone[14], and 2–6 nm thick along [010] direction[9,14], consistent with TEM dark-field observations[15]. This indicates that MPs must be polycrystalline, containing ~10–20 crystals; the flat surface of the platelets must be the sum of the flat surfaces of all the component crystals. The flat or curved morphology of MPs is critical in understanding how MPs are organized with respect to the collagen fibrils and contributes to the stiffness and strength of bone[1].

The crystal chemistry of BA and the similarity of its X-ray diffraction powder patterns to that of apatite[16] have led to it being considered a form of hydroxyapatite, $Ca_5(PO_4)_3(OH)$[17], although broadening of diffraction lines due to the small size of the crystals makes detailed interpretation problematic. Solid-state NMR[18] and Raman spectral analyses[19] show that BA contains no more than ~20% of the OH^- content of hydroxyapatite. FTIR analyses show that it contains significant amounts of CO_3^{2-} and HPO_4^{2-} (see ref.[20]), the former situated both in channel sites and substituting for PO_4^{3-} ions[21]. Based on these results, we could write a general formula for BA as follows: $Ca_{10-x}\square_x[(PO_4)_{6-x}(HPO_4,CO_3)_x]\ (OH_{1-y}\{CO_3\}_y)_{2-x}\square_x$[20,22].

[1]HUN-REN Centre for Energy Research, Konkoly-Thege Miklós u. 29-33, Budapest, Hungary. [2]Department of Mineralogy, Eötvös Loránd University, Pázmány Péter sétány 1/c, Budapest, Hungary. [3]School of Earth, Environment and Society, McMaster University, Hamilton, ON, Canada. [4]School of Biomedical Engineering, McMaster University, Hamilton, ON, Canada. [5]CNRS, Sorbonne Université, Collège de France, Laboratoire Chimie de la Matière Condensée de Paris (LCMCP), F-75005 Paris, France. [6]Department of Rheumatology, Faculty of Medicine, University of Debrecen, Móricz Zsigmond körút 22, Debrecen, Hungary.
✉e-mail: kis.viktoria@ek.hun-ren.hu

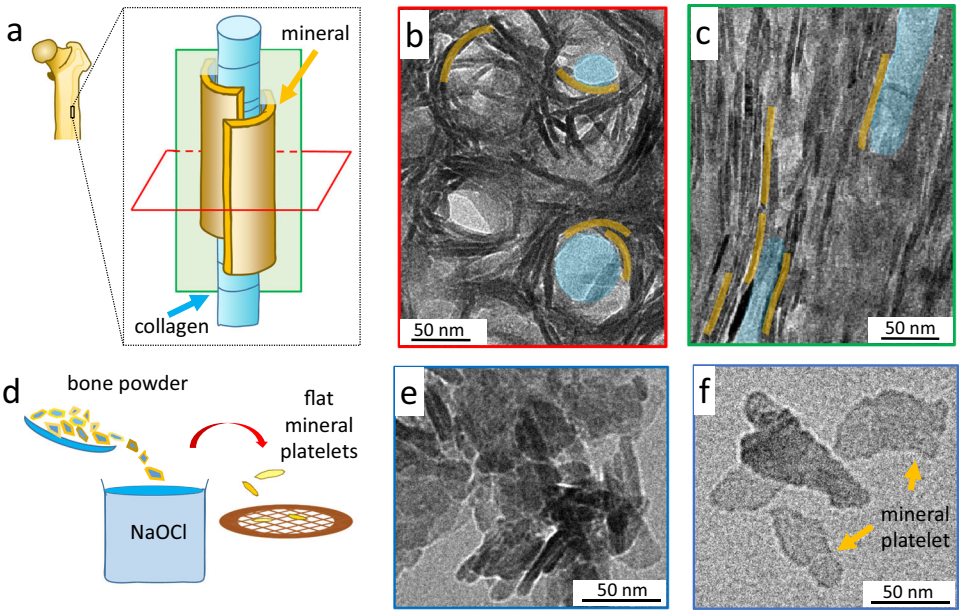

Fig. 1 | Nanocomposite structure of cortical bone. **a** Schematic image of human cortical bone showing MPs curved around collagen fibrils. **b**, **c** Bright field TEM images of cortical bone cut normal (**b**, red plane in (**a**)) and parallel (**c**, green plane in (**a**) to axes of collagen fibrils. Collagen fibrils and curved MPs are indicated with blue and orange, respectively. **d** MPs liberated from bone by oxidation with bleach (NaClO); liberated MPs are no longer curved but lie flat on the TEM grid. **e** Most of them sit in piles of two or more MPs. **f** Some of which are lying uncovered by other fragments, were investigated for crystal symmetry.

Owing to the extremely small size of BA crystals, high-resolution TEM imaging is the only analytical tool, which allows us to determine some aspects of symmetry[23], while not determining its detailed atomic configuration.

Apatite structure is hexagonal with space group $P6_3/m$. Apatite crystals have six identical <100> directions normal to the **c**-axis, resulting in the typical 6-sided hexagonal prism morphology of geological apatite. However, when collagen is removed from bone using an oxidant such as bleach (NaClO), flat plates are liberated[24] (Fig. 1d–f). Flat plate morphology for apatite crystals is quite unusual. These BA plates were shown to be single crystals using electron diffraction[25]; the flat faces were indexed as (10$\bar{1}$0) crystal faces but the four other crystallographically equivalent faces were not visible. This morphology suggests that the actual crystal symmetry of BA is not hexagonal.

Although apatite crystallizes in the hexagonal system (space group $P6_3/m$[16,26]), the space group of stoichiometric hydroxyapatite was shown to be monoclinic, $P2_1/b$[27]. Ma and Liu[28] synthesized monoclinic hydroxyapatite at low temperatures. However, this phase is unlikely to exist in bone since its symmetry depends on the occurrence of OH^- ions alone in a column centered on the **c**-axis whereas BA contains only a small fraction of OH^- ions. Therefore, this cannot explain the lowered symmetry suggested by the form of the BA crystals.

Tao and coworkers[29] raise the question "Why….does apatite, which has a nominal hexagonal symmetry, form platelets with the **c**-axis in the plane of the platelets in violation of the underlying HAP crystallographic symmetry…?". Here, by performing in-depth characterization of bone and related biomimetic mineral, we shed light on the crystallographic basis of the plate-like form by using HRTEM and reveal that multiple crystals exist inside MPs.

Results and discussion

HRTEM analysis of MPs shows small intraplatelet orientation variations

MPs are slightly elongated plates a few tens to hundreds of nm in maximum dimension (Fig. 1e, f). Figure 2a, b shows a separate MP with approximate dimensions of 78 × 46 nm. A low magnification bright field (BF) image (Fig. 2a, inset) of this MP shows that it does not overlap with other platelets. A fast-Fourier transform (FFT) of an area of 66 nm diameter indicates single-crystal character (Fig. 2c). However, atomic resolution (HRTEM) images of 5 × 5 nm adjacent areas show dissimilar patterns (Fig. 2b and Supplementary Fig. S1). Some of these patterns match closely with the crystallographic directions identified on the FFT (Fig. 2c), however, other patterns seem complex, and imply an inhomogeneous atomic structure.

To study the difference between the lattice fringe patterns (Fig. 2b and Fig. S2.1), the corresponding FFTs have been analyzed (Fig. 2d–f). Crystallographic axes and reflection positions on the FFTs taken from the sub-areas coincide with those of an overall FFT (Fig. 2c). However, small disparities in the intensity distributions of the reflections can be seen. For example, Area 1 (Fig. 2d) exhibits a highly symmetric distribution of reflections around the center: the 006 and 00-6 Fourier components are equally present, and reflection rows parallel to the **c***-axis appear in equal numbers on both sides of the axis. In contrast, in Area 2 (Fig. 2e), the 006 and 00-6 peaks are absent (dotted squares) and, at the same time, extra reflection rows appear parallel to **c*** (orange arrows). This indicates that the crystal is slightly tilted approximately around the [210]*-axis.

Reflections on FFT of Fig. 2f exhibit completely different intensity distributions (a pair of strong reflections is marked with yellow circles) while the position of individual reflections still coincides with the position of reflections of the overall FFT (Fig. 2c). Here, the tilt axis of Fig. 2f is outside the image plane. Further examples of orientation variation inside single MPs are provided in Supplementary Figs. S2–S4.

In general, if the electron beam is perpendicular to the platelet and small tilts of some crystals occur around tilt axes lying approximately in the plane of the platelet, reflections of lower Miller indices (low scattering angles) remain at the same position on the FFTs, but with altered intensity distribution. Meanwhile, reflections of larger Miller indices (high scattering angles) may newly appear and others may disappear (for detailed explanation, see section S1.2). FFTs of a large area (tens of nm) average out these small differences and appear symmetric. However, if smaller areas (on the 10 nm scale) are studied separately, orientation variation within a platelet is revealed.

If the tilt axis is parallel to the electron beam, then reflection splitting and, on the HRTEM images, rotational moire patterns can be observed (Supplementary Fig. S3). In these cases, the degree of rotation between two sub-areas can be measured directly on the FFTs, and is always on the order of a few degrees.

Extra reflections in FFTs indicate monoclinic symmetry of crystals

FFT images of several MPs have been analyzed and different [*h*-*k*0] zone axis orientations, e.g., [1–20] (Fig. 2), [1–10] (Supplementary Fig. S2) or [3–20] (Supplementary Fig. S3) were determined. Close

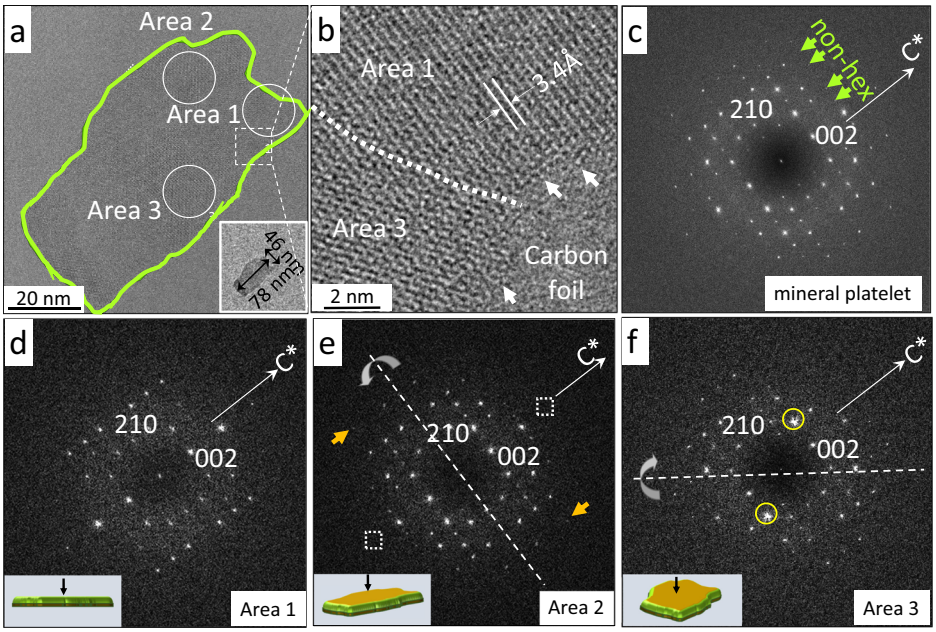

Fig. 2 | Fast Fourier transformation (FFT) analysis of a bone mineral platelet (MP). a HRTEM image of a bone MP with its low magnification bright field image. **b** A small part of the HRTEM image (white square on (**a**)) zoomed in. The boundary between two crystals with slightly different orientation is indicated with a dashed line. The edge of the MP is indicated with white arrows. **c** FFT of the entire MP. Green arrows: extra reflection rows with respect to the hexagonal apatite structure. **d–f** Areas of 16.5 nm diameter, as indicated with white circles on (**a**), exhibiting different lattice fringe patterns, have been analyzed using FFTs. **d** FFT of Area 1 shows a symmetric distribution of reflections around the center. **e** On the FFT of Area 2 two extra rows of reflections appear with respect to (**c**, **b**), as indicated by orange arrows. Missing 006 and 00-6 reflections are indicated with dotted squares. **f** On the FFT of Area 3, while the position of the Fourier spots remains unchanged, the intensity distribution is completely different. Pair of strongest reflections is indicated with yellow. Approximate tilt axis on (**e**) and its projection (**f**) are indicated. The zone axis of this MP would be [1-20] in hexagonal apatite. Drawings of crystals on FFTs illustrate approximate orientation with respect to the electron beam (black arrow).

inspection of these FFTs reveals extra rows of spots, which, based on the hexagonal apatite symmetry $P6_3/m$ (Fig. 3a), cannot be indexed using integers.

For example, extra reflections appear systematically at 1/3 and 2/3 210 in [1–20] zone axis image (green arrows in Figs. 2c and 3b), and at ½ 110 in [1–10] zone axis image (green arrows in Supplementary Fig. S2b and Fig. 3c). Considering a monoclinic unit cell with doubled periodicity along the crystallographic b-axis[27] (Fig. 3a), extra reflections with respect to the hexagonal unit cell could be indexed as shown in Fig. 3f, g. In this case, all [*h*-*k*0] projections, which have been detected can be indexed with a single solution, namely the [110] zone axis orientation of monoclinic apatite. If the crystals are monoclinic, then their flat faces would have Miller indices (010).

Mosaic structure of the MPs shows a mesocrystalline structure

Both measurements in dark-field images[15] and Scherrer analysis of XRD patterns of bone and dentin[13,14] show that the apatite crystals in bone are only about 30 nm in maximum dimension along the *c*-axis, and thus, MPs should be polycrystalline. In TEM sections of bone parallel to collagen fibrils (Fig. 1c) selected area electron diffraction (SAED) images show mutual co-alignment of crystals with a small dispersion[9]. Fig. 1c Therefore, BA nanocrystals in MPs must be co-aligned; this is confirmed by our HRTEM images of single MPs (Fig. 2 and Supplementary Figs. S1–S4). Dark-field images[15] have shown single crystals within MPs with the thicknesses of the MPs themselves, confirming that the MPs mostly consist of single crystals attached edgewise.

Scanning a MP in FFT over an area of 700 nm^2 shows varying crystal orientation; sub-areas can be considered as nanocrystals with different tilt angles with respect to the electron beam, providing a mosaic structure to MPs. Individual nanocrystals are often well distinguishable (e.g., Supplementary Fig. S4). In other cases, only FFT analysis (Supplementary Fig. S2) reveals the subtle variation of crystal orientation inside the MP. Such mosaic-structured "mesocrystals"[30,31] are seen in hematite crystallized from ferrihydrite precursor[32] and in Mg-bearing aragonite[33]. MPs appear to be mesocrystals built of BA nanocrystals aligned along their crystallographic **c**-axes, providing a common outer (010) face, which seems to play an important role in the attachment to the collagen fibrils[29,34] and to other MPs in stacks.

We can visualize the nanocrystals in an MP by performing Fourier filtering on a HRTEM image. The different tilt between the sub-areas is seen on the FFTs, as the varying intensity of 004 reflections (Fig. 2d–f) and the pair of reflections indicated by yellow circles in Fig. 2f. Figure 4 shows the result of the Fourier filtered reconstruction. The shaded area in Fig. 4a represents a nanocrystal, which provides a strong 004 reflection. Shaded areas in Fig. 4b are two other nanocrystals, which provide a pair of dominant *hkl* reflections (Fig. 2f and shown in yellow in the inset of Fig. 4c), indicating a different tilt angle with respect to the electron beam.

In Fig. 4c, the two orientations are plotted together. Overlaps occur because 004 reflections appear all along the MP. However, the variation in its relative intensity with respect to the indicated pair of *hkl* reflections (Fig. 2f) allows us to draw the boundaries of the sub-areas with the same crystal orientation. The component nanocrystals are 30-35 nm wide; edgewise images of MPs do not suggest variation in the thickness at this scale (Figs. 2 and 3 in ref. 1). The mosaic structure of the MPs allows them to flex at the boundaries between the component crystals, enabling MPs to curve and wrap around collagen fibrils (Fig. 1b) as well forming curved structures in the spaces between them[8]. Note that this MP may have been curved inside the bone from which it was extracted (Fig. 1b), which would have increased the angular distances between adjacent sub-areas (crystals).

Shape of bone apatite nanocrystals inside the MPs

The ratio of the length of BA crystals along the *a*- and *c*-axes is 0.47 ± 0.03 as obtained from Scherrer analysis[14], which shows that the crystals are somewhat elongated along the *c*-axis. Fourier transformation of our HRTEM images directly shows that the *c*-axis of the nanocrystals is in the flat plane of the MP[25], and provides an average orientation of the *c*-axis for the whole MP, which also tends to be elongated parallel to this average *c*-axis (Fig. 2a and S4). This contradicts a recently proposed needle-like shape for apatite crystals in bone[34–37]. The surface of the flat plate corresponds to one of the crystallographic (010) faces. This confirms a flat plate morphology of the nanocrystals with differently developed (010) and (100) faces, which is not conformable with hexagonal symmetry.

Unequal development of all the hexagonal facets of apatite crystals was previously interpreted as a result of pseudomorphism after octacalcium phosphate (OCP), a hypothetical crystalline precursor phase of bone

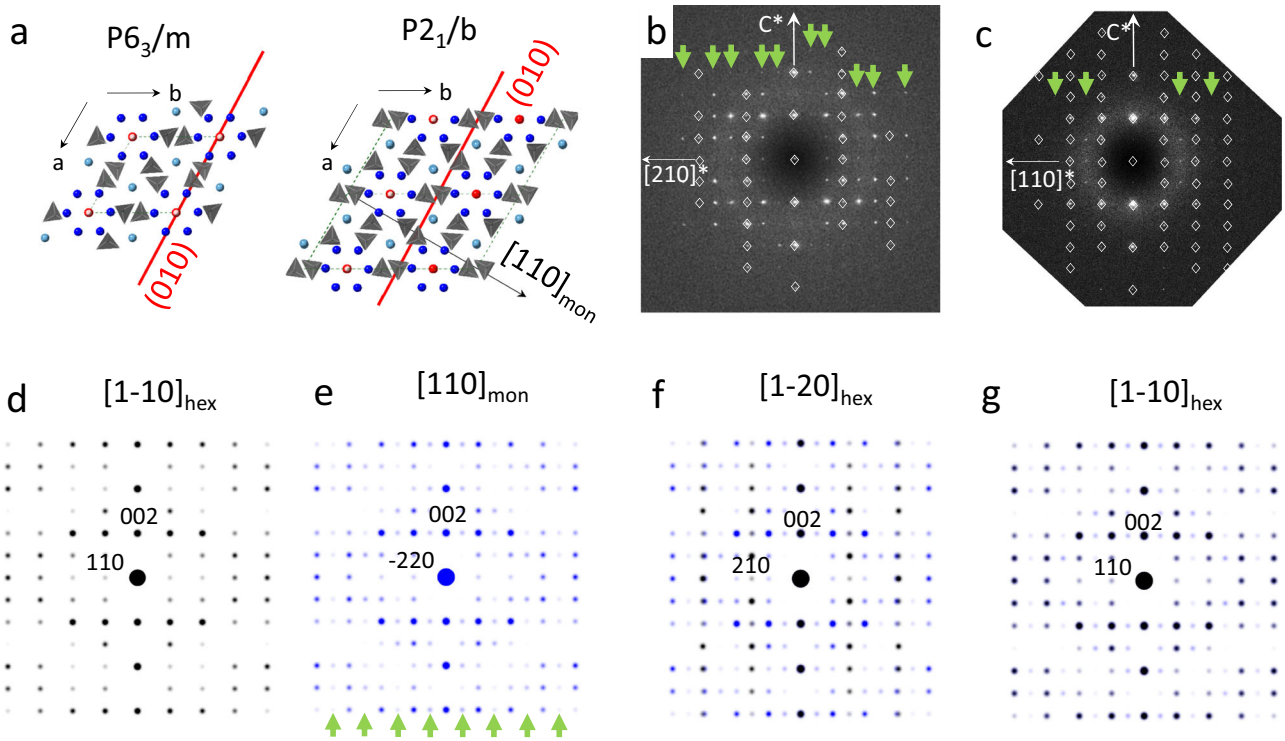

Fig. 3 | Interpretation of extra reflection rows. a Unit cell of hexagonal ($P6_3/m$[52] and monoclinic ($P2_1/b$[27], apatite viewed down the crystallographic *c*-axis. Gray—PO_4 tetrahedra, light and dark blue—Ca1 and Ca2 positions, red+rose – OH group. The rest of the oxygens are omitted for clarity. [110] zone axis of monoclinic apatite is indicated. **b** FFT from Fig. 2c, indexed according to hexagonal apatite unit cell. **c** FFT from Fig. S2.2b, indexed according to hexagonal apatite unit cell. **b**, **c** White diamonds indicate reflections corresponding to the hexagonal cell and green arrows indicate extra rows with respect to the hexagonal cell. **d** Calculated electron diffraction pattern of hexagonal apatite as viewed down the $[1–10]_{hex}$ zone axis. **e** Calculated electron diffraction pattern of monoclinic apatite as viewed down the $[110]_{mon}$ zone axis. Extra rows with respect to hexagonal apatite in (**d**) are indicated with green arrows. **f**, **g** Calculated electron diffraction patterns (black dots) of hexagonal apatite for zone axes $[1–20]_{hex}$ and $[1–10]_{hex}$, corresponding to plane view HRTEM images in (**b**, **c**), respectively. Calculated $[110]_{mon}$ electron diffraction pattern of monoclinic apatite (blue dots) is superimposed. Note that monoclinic symmetry and $[110]_{mon}$ zone axis explains all extra rows indicated on (**b**, **c**).

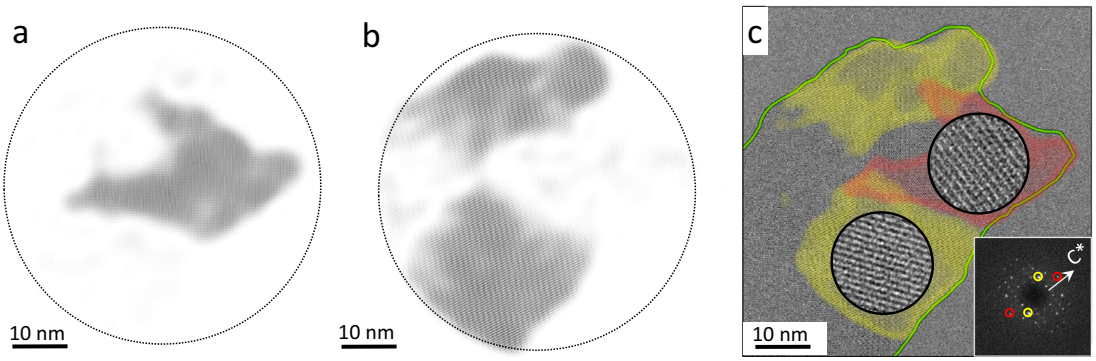

Fig. 4 | Fourier filtered reconstruction of the HRTEM image shown in Fig. 2a. **a** Reconstruction using 004 and 00-4 reflections; and **b** the pair of reflections indicated with yellow in Fig. 2f and in the inset FFT in (**c**). In both (**a**, **b**), a uniform 25% brightness and 75% contrast were applied for a better distinction between the two areas of different orientations. **c** Colored composite image of (**a**) in red, **b** in yellow, and the corresponding part of the original HRTEM. The circles show enlarged HRTEM images displaying different orientation of nanocrystals.

apatite[38,39] of triclinic symmetry. However, the presence of OCP can be easily rejected in bone mineral samples[40] nor does it form during the synthesis of biomimetic apatites in the presence of type I collagen[41,42]. Also, OCP has a different stoichiometry; its formula $Ca_8H_2(PO_4)_6{\cdot}5H_2O$ requires that the Ca/P ratio should be ~1.33, whereas in apatite it is ~1.66 (5/3), while human bone has a typical value of 1.60[43]. Our proposed monoclinic unit cell is inspired by the monoclinic hydroxyapatite structure proposed by Elliott and coworkers[27]. It yields a common indexing solution for all FFTs and a simple and plausible explanation for the typical (010) flat shape of the nanocrystals.

Hydroxyapatite crystallizes in monoclinic symmetry ($P2_1/b$[27]), by ordering of the asymmetric OH^- groups in neighboring channels parallel to the *c*-axis[27]. However, this model for OH^- group ordering cannot apply to BA because: (1) $P2_1/b$ symmetry would require systematic absences of reflections along $[001]_{mon}$* and $[1–10]_{mon}$*, but in our FFT images absences are only observed along $[001]_{mon}$*; (2) this would require stoichiometric amounts of OH^-, whereas only minor amounts exist in BA[18,19]. The complete crystal structure of bone mineral including its space group is still unresolved. The possible role of twinning[44] must be examined. Common

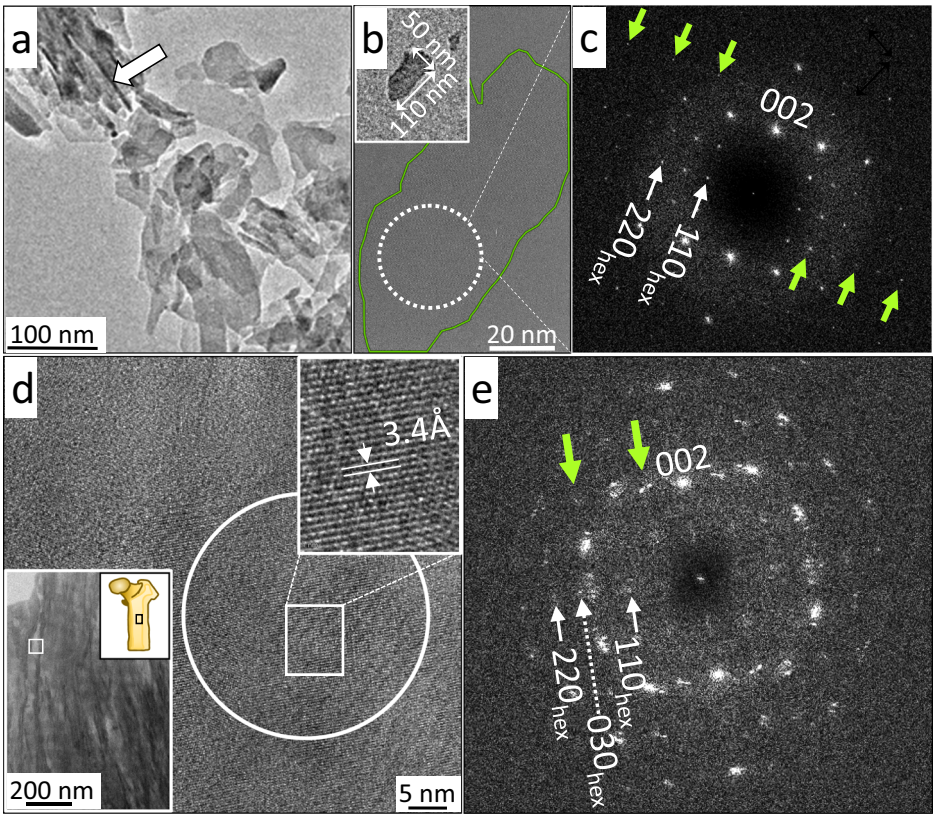

Fig. 5 | Fast Fourier transformation (FFT) analysis of synthetic biomimetic apatite and bone apatite inside bone tissue. a TEM of biomimetic CO_3 apatite platelets lying on a carbon-covered grid; the white arrow shows a single plate viewed edgewise. **b** HRTEM image of a single whole platelet, with the BF image in the inset. **c** Fast-Fourier transform analysis of the area indicated with circle on (**b**). The projection corresponds to $[110]_{mon}$. Extra rows with respect to $[1–10]_{hex}$ are indicated with green arrows. **d**, **e** Correlation of bone morphology with crystallographic directions. **d** HRTEM image of region between two stacks of MPs in a cryo-milled human femur parallel section; bottom left inset: low magnification BF image; upper right inset: magnified image of HRTEM showing lattice fringes normal to *c*-axis, with 3.4 Å spacing corresponding to (002) interplanar distance. **e** FFT taken from the area indicated with a white circle on (**d**). The slight arc shape of the reflections is due to the mosaic character of the MPs. The average orientation of the MP is $[110]_{mon}$. Green arrows indicate extra reflection rows with respect to the hexagonal structure, characteristic of monoclinic apatite. The weak reflection indicated as 030_{hex} comes from another crystallite in [100] orientation ($[100]_{mon}$ and $[100]_{hex}$ projections coincide).

structure motifs seen in OCP and HAP might also serve as good starting points.

On X-ray diffraction powder patterns taken from bone, no additional reflections characteristic of the monoclinic symmetry appear (e.g., ref. 16). This might be related to the extensive broadening of diffraction peaks due to the small crystal size, which obscures detection of low-intensity reflections. Elliott et al.[27] show that the intensity of these extra reflections would not exceed 1.5%.

Synthetic, biomimetic apatite

Nassif et al.[45] synthesized a carbonated apatite similar to bone mineral[46], which forms platelets that are about 5–10 nm thick (Fig. 5a, b) and has recently been used successfully for bone regeneration[4]. HRTEM images of this biomimetic apatite yield FFT patterns (Fig. 5c) with the same additional rows of reflections as seen in bone mineral, indicating that it has a monoclinic structure. The FFT reflections are noticeably sharper here than in bone mineral, indicating a better-ordered atomic structure. Scherrer analysis of XRD shows that the crystals are 50 nm long along the *c*-axis[45].

Organization of monoclinic bone apatite crystals inside bone tissue

To complement our improved understanding of the crystal morphology and their monoclinic symmetry inside MPs, it is also useful to identify these characteristics in a TEM section of bone. The upper inset of Fig. 5d shows a FIB section of human femoral cortical bone oriented so that the CF axes lie in the plane of the section. Stacks of co-aligned MPs viewed edgewise are spaced about 40 nm apart, perpendicular to the fainter 67-nm-spaced gap zones of the CFs. The CF axis must be perpendicular to the zone boundaries and therefore parallel to the MPs stacks, lying in the plane of the image. Between each stack of MPs in a parallel section, we are looking through a CF, which is continuously surrounded by MPs, as logically follows from cross sectional views (Fig. 1a). In BF images of parallel sections, the surrounding MPs, which lie in the plane of the section, are unresolved (Figs. 1b and 5d, lower inset). We are viewing them normal to the (010) plane as confirmed by an HRTEM image of a region between two MPs stacks (Fig. 5d). The HRTEM image shows 0.34 nm-spaced layer lines oriented normal to the *c*-axis of the apatite crystals. On the FFT of the area inside the white circle (Fig. 5e), the additional reflection rows parallel to the [001]* axis, indicative of monoclinic symmetry, are clearly distinguished. This image confirms that the monoclinic apatite crystals of the MPs are oriented in mineralized bone with their *c*-axis aligned parallel to the collagen fibrils.

Conclusions

From our study, we have made two new observations about the ultrastructure of bone.

First, we show that MPs are mosaics of apatite crystals about 30-35 nm across, whose **c**-axes are approximately parallel to one another, but in slightly different orientations. The orientation difference of the crystals does not exceed a few degrees, so that in an HRTEM image of an MP, we obtain an FFT pattern resembling that of a single hexagonal crystal with its *c*-axis oriented parallel to the longer dimension of the plate. As MPs in bone tissue are curved, we infer that the difference in angle between adjacent crystals could have been larger. The mosaic of multiple crystals explains previous observations using both dark-field TEM and XRD, showing that MPs are polycrystalline aggregates of ~30 nm wide crystals of apatite. The flat plate of the MPs, which can face towards a collagen fibril or a neighboring MP, forms by the oriented attachment of several (010) crystal faces. The mosaic structure and related flexibility allow MPs to curve and wrap around collagen fibrils.

We also found, in the FFT pattern of individual apatite crystals, rows of spots parallel to the *c*-axis not expected for a hexagonal structure but consistent with the crystals having a monoclinic symmetry. We infer from this that the Ca phosphate crystals in bone are monoclinic rather than hexagonal, in contrast to most apatite group minerals. This accounts for their plate-like form in bone and dentin. We also show that the same monoclinic

structure appears in plate-like crystals of biomimetic apatite[45] used successfully for bone regeneration[4].

These two sets of observations significantly modify our understanding of the structure of the mineral component of bone. It had been previously shown that the fundamental mineral structures in bone at the nanometer scale are stacks of up to 30 MPs deformed into curved cylindrical structures[8]. These structures provide most of the strength of bone since collagen is a weak material. Now we see more clearly how the symmetry and shape of the bone apatite nanocrystals allow them to be assembled into these plate-like sheets whose structural characteristics, both individually and in stacks[47], contributes to the strength and toughness of bone. This knowledge may also be helpful for the development of biomimetic materials and improved biomedical implants.

Methods

Bone samples

Fragments of bone were harvested from the skeleton of an adult female sheep (*Ovis aries*). IMM-Recherche received ethical approval from the Direction Départementale de la Protection des Populations (n°75-14-01) for experiments related to the use of sheep bone in this study. The Scientific and Research Ethics Committee of Debrecen University gave ethical approval for the experiments on the human bone sample (approval no. 37597-1/2012/EKU). The composition of the mineral in the sheep bone sample was determined to be $Ca_{7.5}(PO_4)_{2.8}(HPO_4)_{2.6}(CO_3)_{0.6}(OH)_{0.2}$[48].

Sample preparation for TEM

Deproteinized MPs. Fresh fragments of cortical bone were ground in an agate mortar. Mineral was extracted following method 2 reported by Weiner and Price[24]. In brief, the powder was sonicated in 10 ml of cold dilute NaClO (pH ~9.6) and centrifuged, and the residue was then ground further. This procedure was repeated three times. Overall, the treatment with NaClO solution lasted 4 h. The sample was then washed three times in distilled water, twice with 95% ethanol, once with sonication for 15 min in 100% ethanol, and dried at 37 °C for 3 days. Powdered bone was suspended in ethanol and ultrasonicated for at least 1 min. Afterward, 0.5 µl of the suspension was deposited on a 3-nm-thick lacey carbon film on a Cu grid (Ted Pella) and the liquid was left to evaporate.

Cryo Ar^+ milled samples. To study the MPs in situ in the bone tissue, human cortical bone (femur, 72-year-old deceased female) has been investigated. Clinical parameters of the bone sample are normal considering the age of the individual; no pathological deviations were detected.

A TEM sample was prepared by cryo Ar^+-ion milling[9]. Oriented blocks of bone of 1.5 mm × 1.5 mm have been embedded in G1 epoxy resin (Gatan Inc.), left for at least 24 h to infiltrate the block, which was fixed with the same resin into a 3 mm diameter TEM Ti disc. Mechanical polishing was performed down to 70 µm thickness. Then the sample was thinned using a Technoorg Linda Ar^+ ion thinner from both sides of the disk, with 6 keV and 2 mA, and at the end with 3 keV, 1 mA. During Ar^+ ion thinning, LN_2 cooling was applied. The electron-transparent sample was coated with a thin amorphous carbon layer before TEM study (Fig. 1).

HRTEM imaging

TEM study was performed using an FEI Themis G2 Cs corrected microscope (FEI, Thermo Fischer, Schottky FEG electron source) equipped with a four-segment Super-X EDS detector. During the measurements 200 keV accelerating voltage was applied, which allows 0.08 nm resolution in high-resolution (HRTEM) mode and 1.6 nm resolution in scanning (STEM) mode. HRTEM images were recorded with a 4k × 4k Ceta camera using Velox software (Themo Fischer). Bone mineral is highly sensitive to electron irradiation, and thus special care was taken not to induce beam damage. The stability of hydroxyapatite nanoparticles, similar in composition and structure to bone mineral, during HRTEM analysis was studied in several papers, and changes in symmetry[49,50] and the formation of voids and mosaic structure[51] reported. To minimize such effects, we decreased beam interaction by using a small electron beam spot size. Also, a beam blank was applied when a change of magnification range induced transients with high beam intensity. We tested the stability of the structure at the applied experimental conditions (typical screen current values 700–1000 pA); formation of mosaic structure was observed only after 5 min of beam exposure. All HRTEM images analyzed during the study were recorded within this time limit.

Due to the high resolution of the camera and the large unit cell of apatite (a_0 = 9.44 Å, c_0 = 6.878 Å) interplanar distances can be resolved at relatively low magnifications, ranging in this study from 170,000 to 350,000x. It allows lattice resolution imaging of whole MPs (~60–120 nm in size) on a single HRTEM image. HRTEM images display periodic bright and dark features are called lattice fringes, with spacings corresponding to interplanar distances (*d*-values) of the crystal. FFT analysis of the HRTEM produces a pattern of sharp spots called Fourier maxima, which resemble single-crystal electron diffraction pattern peaks. Indexing FFTs allows us to determine zone axis orientation of the crystal on the HRTEM image and an accurate measurement of interplanar distances. In case of thin films or thin crystals due to the finite size, reciprocal lattice points, and thus diffraction spots are elongated perpendicular to the thinnest dimension ("diffraction spikes"). The intensity along a diffraction spike is not uniform, it decreases as the distance between the detector plane and the Ewald sphere increases. The elongated shape of the diffraction spots allows us to obtain images at atomic resolution even if the orientation of the nanocrystal is slightly tilted out of zone axis, in case the tilt axis is in, or close to the image plane. In this case, the intensity of the spots will change as a function of the tilt angle with respect to the image plane. Thus, the intensities of symmetrically related FFT maxima can be unequal, and, with increasing tilt, reflections at high scattering angle far from the tilt axis can disappear, and new reflections at high scattering angle close to the tilt axis can appear. Zone axis orientation, tilt, and crystal symmetry were determined using FFT analysis using CRISP software (Calidris, Sollentuna, Sweden).

Data availability

The data that support the findings of this study are available from the corresponding author upon reasonable request.

Received: 2 April 2025; Accepted: 15 July 2025;
Published online: 20 August 2025

References

1. Schwarcz, H. P., Abueidda, D. & Jasiuk, I. The ultrastructure of bone and its relevance to mechanical properties. *Front. Phys.* **5**, 39 (2017).
2. Wegst, U. G. K., Bai, H., Saiz, E., Tomsia, A. P. & Ritchie, R. O. Bioinspired structural materials. *Nat. Mater.* **14**, 23–36 (2015).
3. Feng, P. et al. Structural and functional adaptive artificial bone: materials, fabrications, and properties. *Adv. Funct. Mater.* **33**, 1–29 (2023).
4. Robin, M. et al. Mineralized collagen plywood contributes to bone autograft performance. *Nature* **636**, 100–107 (2024).
5. Jager, I. & Fratzl, P. Mineralized collagen fibrils: a mechanical model with a staggered arrangement of mineral particles. *Biophys. J.* **79**, 1737–1746 (2000).
6. Tertuliano, O. A. & Greer, J. R. The nanocomposite nature of bone drives it strength and damage resistance. *Nat. Mater.* **15**, 1195–1203 (2016).
7. Schwarcz, H. P. The ultrastructure of bone as revealed in electron microscopy of ion-milled sections. *Semin. Cell Dev. Biol.* **46**, 44–50 (2015).
8. Schwarcz, H. P., Nassif, N. & Kis, V. K. Curved mineral platelets in bone. *Acta Biomater.* **183**, 201–209 (2024).
9. McNally, E., Schwarcz, H., Botton, G. & Arsenault, A. A model for the ultrastructure of bone based on electron microscopy of ion-milled sections. *PLoS ONE* **7**, e29258 (2012).

10. Grandfield, K., Vuong, V. & Schwarcz, H. P. Ultrastructure of bone: hierarchical features from nanometer to micrometer scale revealed in focused ion beam sections in the TEM. *Calcif. Tissue Int.* **103**, 606–616 (2018).
11. Lee, B. E. J., Luo, L., Grandfield, K., Andrei, C. M. & Schwarcz, H. P. Identification of collagen fibrils in cross sections of bone by electron energy loss spectroscopy (EELS). *Micron* **124**, 102706 (2019).
12. Micheletti, C., Shah, F. A., Palmquist, A. & Grandfield, K. Ultrastructure and nanoporosity of human bone shown with correlative on-axis electron and spectroscopic tomographies. *ACS Nano* **17**, 24710–24724 (2023).
13. Forien, J.-B. et al. X-ray diffraction and in situ pressurization of dentine apatite reveals nanocrystal modulus stiffening upon carbonate removal. *Acta Biomater.* **120**, 91–103 (2021).
14. Turunen, M. J. et al. Bone mineral crystal size and organization vary across mature rat bone cortex. *J. Struct. Biol.* **195**, 337–344 (2016).
15. Schwarcz, H. P., McNally, E. A. & Botton, G. A. Dark-field transmission electron microscopy of cortical bone reveals details of extrafibrillar crystals. *J. Struct. Biol.* **188**, 240–248 (2014).
16. Wenk, H. R. & Heidelbach, F. Crystal alignment of carbonated apatite in bone and calcified tendon: results from quantitative texture analysis. *Bone* **24**, 361–369 (1999).
17. Elliott, J. C. Calcium phosphate biominerals. *Rev. Mineral. Geochem.* **48**, 427–453 (2002).
18. Cho, G., Wu, Y. & Ackerman, J. L. Detection of hydroxyl ions in bone mineral by solid-state NMR spectroscopy. *Science* **300**, 1123–1127 (2003).
19. Pasteris, J. D. et al. Lack of OH in nanocrystalline apatite as a function of degree of atomic order: implications for bone and biomaterials. *Biomaterials* **25**, 229–238 (2004).
20. Spevak, L., Flach, C. R., Hunter, T., Mendelsohn, R. & Boskey, A. Fourier transform infrared spectroscopic imaging parameters describing acid phosphate substitution in biologic hydroxyapatite. *Calcif. Tissue Int.* **92**, 418–428 (2013).
21. Madupalli, H., Pavan, B. & Tecklenburg, M. M. J. Carbonate substitution in the mineral component of bone: discriminating the structural changes, simultaneously imposed by carbonate in A and B sites of apatite. *J. Solid State Chem.* **255**, 27–35 (2017).
22. Cazalbou, S., Combes, C., Eichert, D. & Rey, C. Adaptative physico-chemistry of bio-related calcium phosphates. *J. Mater. Chem.* **14**, 2148–2153 (2004).
23. Kis, V. K., Czigány, Z., Dallos, Z., Nagy, D. & Dódony, I. HRTEM study of individual bone apatite nanocrystals reveals symmetry reduction with respect to P63/m apatite. *Mater. Sci. Eng. C.* **104**, 109966 (2019).
24. Weiner, S. & Price, P. A. Disaggregation of bone into crystals. *Calcif. Tissue Int.* **39**, 365–375 (1986).
25. Moradian-Oldak, J., Weiner, S., Addadi, L., Landis, W. J. & Traub, W. Electron imaging and diffraction study of individual crystals of bone, mineralized tendon and synthetic carbonate apatite. *Connect. Tissue Res.* **25**, 219–228 (1991).
26. Voltolini, M., Wenk, H., Barreiro, G. & Sabrina, C. Hydroxylapatite lattice preferred orientation in bone: a study of macaque, human and bovine samples research papers. *Appl. Crystallogr.* **44**, 928–934 (2011).
27. Elliott, J., Mackie, P. & Young, R. Monoclinic apatite. *Science* **180**, 1055–1057 (1973).
28. Ma, G. & Liu, X. Y. Hydroxyapatite: hexagonal or monoclinic?. *Cryst. Growth Des.* **9**, 2991–2994 (2009).
29. Tao, J. et al. Energetic basis for the molecular-scale organization of bone. *Proc. Natl. Acad. Sci. USA* **112**, 326–331 (2015).
30. Cölfen, H. & Antonietti, M. Mesocrystals: inorganic superstructures made by highly parallel crystallization and controlled alignment. *Angew. Chem. Int. Ed.* **44**, 5576–5591 (2005).
31. Jehannin, M., Rao, A. & Cölfen, H. New horizons of nonclassical crystallization. *J. Am. Chem. Soc.* **141**, 10120–10136 (2019).
32. Zhu, G. et al. Self-similar mesocrystals form via interface-driven nucleation and assembly. *Nature* **590**, 416–422 (2021).
33. Molnár, Z., Pekker, P., Rečnik, A. & Pósfai, M. Formation and properties of spindle-shaped aragonite mesocrystals from Mg-bearing solutions. *Nanoscale* **16**, 2012–2021 (2024).
34. Xin, R., Leng, X. & Wang, N. HRTEM study of the mineral phases in human cortical bone. *Adv. Eng. Mater.* **12**, B552–B557 (2010).
35. Fratzl, P., Schreiber, S. & Klaushofer, K. Bone mineralization as studied by small-angle X-ray scattering. *Connect. Tissue Res.* **34**, 247–254 (1996).
36. Xu, Y. F. et al. Intermolecular channels direct crystal orientation in mineralized collagen. *Nat. Comm.* **11**, 1–12 (2020).
37. Reznikov, N., Bilton, M., Lari, L., Stevens, M. M. & Kröger, R. Fractal-like hierarchical organization of bone begins at the nanoscale. *Science* **360**, eaao2189 (2018).
38. Brown, W. E. & Chow, L. C. Chemical properties of bone mineral. *Annu. Rev. Mater. Sci.* **6**, 213–236 (1976).
39. Davies, E. et al. 2014. Citrate bridges between mineral platelets in bone. *Proc. Natl. Acad. Sci. USA* **111**, E1354–E1363 (2014).
40. Rey, C., Combes, C., Drouet, C. & Glimcher, M. J. Bone mineral: update on chemical composition and structure. *Osteoporos. Int* **20**, 1013–1021 (2009).
41. Nudelman, F. et al. The role of collagen in bone apatite formation in the presence of hydroxyapatite nucleation inhibitors. *Nat. Mater.* **9**, 1004–1009 (2010).
42. Wang, Y. et al. The predominant role of collagen in the nucleation, growth, structure and orientation of bone apatite. *Nat. Mater.* **11**, 724–733 (2012).
43. Shah, F. Revisiting the physical and chemical nature of the mineral component. *Acta Biomaterialia* **196**, 1–16 (2025).
44. Aquilano, D., Bruno, M., Rubbo, M., Massaro, F. R. & Pastero, L. Low symmetry polymorph of hydroxyapatite. Theoretical equilibrium morphology of the monoclinic $Ca_5(OH)(PO_4)_3$. *Cryst. Growth Des.* **14**, 2846–2852 (2014).
45. Nassif, N. et al. In vivo inspired conditions to synthesize biomimetic hydroxyapatite. *Chem. Mater.* **22**, 3653–3663 (2010).
46. Wang, Y. et al. Impact of collagen confinement vs. ionic substitutions on the local disorder in bone and biomimetic apatites. *Mater. Horiz.* **2**, 224–231 (2014).
47. Pang, S., Schwarcz, H. P. & Jasiuk, I. I. Interfacial bonding between mineral platelets in bone and its effect on mechanical properties of bone. *J. Mech. Behav. Biomed. Mater.* **113**, 104132 (2021).
48. Von Euw, S. et al. Bone mineral: new insights into its chemical composition. *Sci. Rep.* **9**, 8456 (2019).
49. Henning, P. A., Landa-Cánovas, A. R., Larsson, A. K. & Lidin, S. Elucidation of the crystal structure of oxyapatite by high-resolution electron microscopy. *Acta Crystallogr. Sect. B Struct. Sci.* **55**, 170–176 (1999).
50. Nicolopoulos, S. et al. Characterization by TEM of local crystalline changes during irradiation damage of hydroxyapatite compounds. *J. Solid State Chem.* **116**, 265–274 (1995).
51. Reyes-Gasga, J., Garcia-Garcia, R. & Brès, E. Electron beam interaction, damage and reconstruction of hydroxyapatite. *Phys. B Condens. Matter* **404**, 1867–1873 (2009).
52. Hughes, J. M., Cameron, M. & Crowley, K. D. Structural variations in natural F, OH, and Cl apatites. *Am. Mineral.* **74**, 870–876 (1989).

Acknowledgements

The authors acknowledge discussions with Prof. István Dódony (Környe, Hungary) and Prof. György Radnóczi (HUN-REN Centre for Energy Research, Budapest, Hungary) and critical comments on the first draft by Dr. Zsolt Czigány (HUN-REN Centre for Energy Research, Budapest, Hungary). Preparation of TEM samples was assisted by Ms. Andrea Fenyvesi-Jakab. Research support: Funding for some aspects of this study was provided by the National Research, Development and Innovation Fund Office, Hungary,

grant number K-125100 (V.K.K.). The electron microscopy facility at the Centre for Energy Research was granted by the European Structural and Investment Funds, grant no. VEKOP-2.3.3–15–2016–0 0 0 02.

Author contributions

V.K.K. conducted TEM sample preparation and experiments, analyzed data, and interpreted experimental results. V.K.K. wrote the original manuscript in collaboration with H.P.S., and with contribution from N.N. H.P.S. promoted the idea of HRTEM study of mineral platelets. N.N. supplied the sheep bone and the biomimetic apatite samples, and prepared some of the samples. N.N. was actively involved in the discussion and interpretation of the results. Z.Sz. supplied the human sample and performed evaluation of clinical parameters. All authors contributed to the review and editing.

Funding

Open access funding provided by HUN-REN Centre for Energy Research.

Competing interests

The authors declare no competing interests.

Additional information

Supplementary information The online version contains supplementary material available at https://doi.org/10.1038/s43246-025-00890-4.

Correspondence and requests for materials should be addressed to Viktória K. Kis.

Peer review information *Communications Materials* thanks the anonymous reviewers for their contribution to the peer review of this work. Primary Handling Editors: Jet-Sing Lee. [A peer review file is available].